Ultrahigh-pressure generation using light-ion beams

A. Ng and A. R. Piriz*
Department of Physics, University of British Columbia, Vancouver, British Columbia, Canada V6T 2A6
(Received 2 September 1988; revised manuscript received 30 March 1989)

Using a simple analytical model, we examined the process of ultrahigh-pressure generation using ion-beam-driven flyers to impact on a stationary sample. The results suggested that pressures in excess of 5 Mbars can be attained in materials of medium densities even for a beam power density of 10^{11} W/cm^2 that is readily available with existing machines. This, together with the mm-size diameter of the ion beam on target and the lack of a high-temperature plasma corona, renders light-ion beams potentially a most powerful tool for laboratory high-pressure research.

Research at high pressure is not only of fundamental interest in condensed-matter physics, but also of great importance to the study of geophysics and planetary science, as well as inertial confinement fusion. Static pressures up to ~5 Mbars can be achieved in diamond-anvil cells.[1] Alternatively, dynamic pressures of similar magnitudes can be attained in impact experiments using high explosives[2] or gas guns.[3] Until recently, higher pressures could only be produced in nuclear explosions.[4] The advent of high-power lasers has led to the production of shock waves with pressures in excess of 5 Mbars via laser-driven ablation of solids,[5-8] providing a unique laboratory access to the ultrahigh-pressure regime. On the other hand, the use of light-ion beams to generate shocks has also been well recognized and explored for the implusion of inertial confinement fusion targets.[9] The classical energy deposition process of light ions in solids avoids many of the deleterious effects associated with laser-induced parametric instabilities, while the lack of a high-temperature (~keV) plasma corona characteristic of laser-heated targets greatly mitigates radiative preheat, particularly for high-Z materials. Of particular importance to high-pressure studies, the inherent large irradiation area (~mm size) and uniformity of pressure generation render light-ion beams an attractive tool for producing planar shock waves. Unfortunately, the focusability of the beam also constrains the irradiance to $\leq 10^{11}$ W/cm^2, resulting in a shock pressure of ≤ 1 Mbar.[10,11] However, this pressure limit stems from the use of the thermal pressure generated by ion-energy deposition in the absorber region of the target to drive a shock into its payload. A much higher shock pressure can be achieved by adopting the well-known flyer-impact technique,[12] whereby the expansion of the absorber is used to propel the payload, which then impacts on the sample of interest. In this work, through a simple analytical model, we have explored and illustrated the use of light-ion beams for flyer accelerations. With proper target designs, pressures in access of 5 Mbars can be readily attained with existing machines thus making light-ion beams a viable means for research in the ultrahigh-pressure regime.

An earlier model, which treated the expansion of a uniform target,[13] was extended to the more general case of a nonuniform target comprising an external tamper, an internal absorber, and a payload (Fig. 1). The beam energy was assumed to be uniformly and completely deposited in the tamper and internal absorber. The subsequent expansions of these heated regions were such that the center-of-mass surface of the target remained at rest. This greatly simplified the model and appeared to be a reasonable approximation as indicated by hydrodynamic simulations.[14-16] The velocity profiles in the tamper and internal absorber were assumed to be linear, although the slope of each profile could be different and could vary with time (Fig. 2). For relatively long times, the slopes would become the same in both regions,[17,18] while for short times they were functions of the absorbed energy per unit mass.[19] In the following calculation, we have taken the same linear velocity profile in the tamper and the internal absorber.

The dynamics of the payload is more complex. The thermal pressure generated in the internal absorber will drive a shock wave into the payload. The shocked material is accelerated and compressed. Both the pressure and the particle velocity are continuous across the absorber-payload interface. The shock will continue to propagate until it reaches the free surface of the payload, where a rarefaction wave will be produced. For a sufficiently thick payload, the shock transit time is of the order of the pulse duration of the ion beam and the effect of the rarefaction wave is not considered. This represents the well-studied shock regime in high-pressure generation by ion beams.[20-22] For a thin payload, the rarefaction wave plays an important role in its dynamics. When this backward-propagating wave arrives at the interface be-

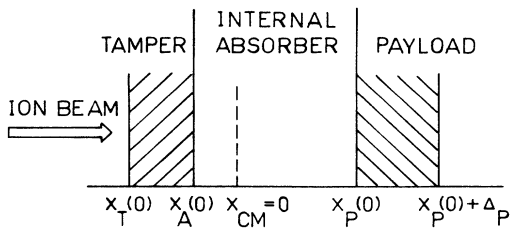

FIG. 1. Schematics of an ion-beam target. The coordinates correspond to initial conditions.

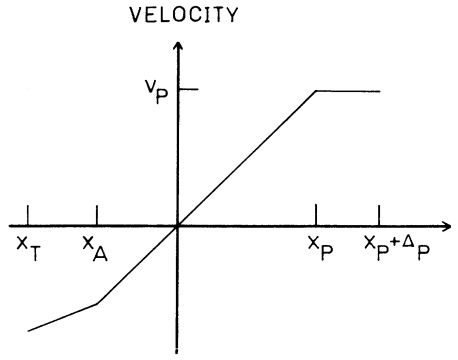

FIG. 2. Instantaneous velocity profiles in target.

tween the internal absorber and the payload, a new shock is launched that will recompress the expanding payload. If the payload is sufficiently thin, this process of alternating shock and rarefaction will be repeated and in a time of the order of few acoustic transit times, the pressure profile in the payload will relax to one in which the pressure varies continuously from that at the absorber-payload interface to zero at the free surface of the payload. The particle velocity in the payload becomes uniform, which can be used as an accelerated flyer to impact on a sample. In this work, we will consider only such flyer regimes. Since the ion-energy deposition is uniform in both the tamper and the internal absorber, the energy E_A of the ions arriving at the absorber is[14,15,18,19,22]

$$E_A = E_0[1-(\rho_T d_T/R_T)] , \tag{1}$$

where E_0 is the ion-beam energy, ρ_T is the tamper density, d_T is the tamper thickness, and $R_T = R_T(E_0)$ is the ion range in units of areal density (g/cm^2) in the tamper. It may be noted that uniform deposition is a better approximation for heavy ion beams than for proton beams, since the latter exhibit a Bragg peak in the energy deposition profile when the temperature of the absorber is zero. However, as the absorber temperature increases, the Bragg peak is removed and the approximation of uniform deposition improves. In any case, such an approximation yields a pessimistic estimate of the tamping effect because the existence of a Bragg peak allows more energy to be deposited in the internal region of the absorber. For simplicity, the range in the internal absorber will be taken as a power law,

$$R_A(E_A) = aE_A^b , \tag{2}$$

where the coefficients a and b are determined from tabulated data.[23–26] Since the beam must be stopped when it reaches the payload, $\rho_A d_A = R_A(E_A)$, where ρ_A is the internal absorber density an d_A is its thickness. Thus we have

$$\rho_A d_A = aE_0^b[1-(\rho_T d_T/R_T)]^b . \tag{3}$$

The dynamics of the target will then be described by an equation of conservation of energy, which can be obtained by integrating the fluid equations between $x=0$ (the center-of-mass surface) and $x = x_P + \Delta_P$ (see Fig. 2). Following the previous model,[13] the total kinetic energy in this region can be written as

$$\tfrac{1}{2}\int_0^{x_P+\Delta_P} \rho v^2 dx = E_{kp} + E_{k\,\mathrm{abs}} = (1+F)\frac{m_P v_P^2}{2} , \tag{4}$$

where m_P is the payload mass in units of areal density (g/cm^2), $E_{kp} = \frac{1}{2} m_P v_P^2$ is the kinetic energy of the payload, and $E_{k\,\mathrm{abs}}$ is the kinetic energy of the internal absorber. $F = E_{k\,\mathrm{abs}}/E_{kP}$ can be found from the integral in Eq. (4) to be[13]

$$F = \frac{\rho_A x_P(0)}{\kappa m_P}\left[1 + H((x_P(0)-d_A) \times \left[\frac{\rho_T}{\rho_A}-1\right]\left[1-\frac{d_A}{x_P(0)}\right]^3\right] , \tag{5}$$

where

$$H(z) = \begin{cases} 0 & \text{if } z \le 0 \\ 1 & \text{if } z \ge 0 \end{cases}$$

is the Heaviside unit function and κ is a parameter dependent on the density profile in the internal absorber region. This density profile is known in the limiting cases. For large payload mass, the density in the internal absorber tends to be uniform[13] and $\kappa = 3$. In the limit of $m_P \to 0$, the absorber density profile becomes Gaussian[18] and $\kappa = 2$. The value of κ is not very sensitive to the density profile of the internal absorber and any value $2 \le \kappa \le 3$ can be chosen without affecting the results appreciably. For the flyer acceleration process (m_P small), we have taken $\kappa = 2$.

The instantaneous position x_P and velocity v_P of the payload are then given by

$$\frac{d}{dt}\left[(1+F)m_P\left[\frac{v_P^2}{2}+\frac{x_P}{\gamma-1}\frac{dv_P}{dt}\right]\right] = \alpha W(t) , \tag{6}$$

where γ is the enthalpy coefficient and $W(t)$ is the ion-beam power density. α is the fraction of the beam energy deposited in the region $0 \le x \le x_P$ given by

$$\alpha = \begin{cases} (1-m_T/R_T)[x_P(0)/d_A] & \text{if } d_A \ge x_P(0) \\ 1-\{\rho_T[d_A+d_T-x_P(0)]/R_T\} & \text{if } d_A \le x_P(0), \end{cases} \tag{7}$$

where $m_T = \rho_T d_T$ is the tamper mass in units of areal density (g/cm^2). The initial conditions for Eq. (6) are $x_P(t=0) = x_P(0)$ and $v_P(t=0) = 0$.

Here, we considered a square pulse of ion beam with constant power density W_0 in a duration t_B. This sample case was chosen for the sake of simplicity. The exact pulse shape could be used readily if such information becomes available for any specific ion-beam machines. (Considering the 2-ns rise time typical of a second-generation, 100-TW machine,[27] a square pulse appears to be a reasonable approximation when the pulse duration is ≥ 20 ns.) Accordingly, Eq. (6) can be integrated to yield

$$(1+F)\frac{m_P}{2}\left[v_P^2+3x_P\frac{dv_P}{dt}\right] = \alpha W_0[t+(t_B-t)H(t-t_B)] , \tag{8}$$

for $\gamma=\frac{5}{3}$. Introducing the following dimensionless variables

$$\xi=x_P/x_P(0)\ , \tag{9}$$

$$T=t/t_0,\quad t_0=[(1+F)m_P x_P^2(0)/2\alpha W_0]^{1/3}\ , \tag{10}$$

Eq. (8) can be written as

$$\ddot{\xi}=\frac{T+(T_B-T)H(T-T_B)-\dot{\xi}^2}{3\xi}\ . \tag{11}$$

The dot indicates derivatives with respect to T and $T_B=t_B/t_0$. The initial conditions become $\xi(T=0)=1$ and $\dot{\xi}(T=0)=0$.

A useful figure of merit for this flyer-acceleration process is the hydrodynamic efficiency η_H defined as

$$\eta_H=m_P v_P^2/2W_0 t_B\ , \tag{12a}$$

or, in dimensionless variables,

$$\eta_H=\frac{\alpha}{1+F}\frac{\dot{\xi}^2}{T_B}\ . \tag{12b}$$

It may be noted that as $m_P\to 0$, $\eta_H\to 0$ and v_P approaches the sound speed.[13] On the other hand, the pressure exerted on the payload due to thermal expansion of the internal absorber can be obtained from the boundary condition

$$p_P=m_P\frac{dv_P}{dt}\ , \tag{13}$$

or, in dimensionless variables,

$$P=p_P/p_0=\ddot{\xi}\ , \tag{14}$$

where p_0 is defined as

$$p_0=[m_P/x_P(0)]^{1/3}[2\alpha W_0/(1+F)]^{2/3}\ . \tag{15}$$

Detailed derivations of the equations have been described elsewhere.[13] To obtain the complete solution for the dynamics of the payload, Eq. (11) is integrated numerically. In Fig. 3, we present the results for the dimensionless pressure $P(T)$ and the dimensionless velocity $\dot{\xi}(T)$. The pressure exerted on the payload reaches its maximum value of $\sim 0.4p_0$ at $t\approx 2t_0$. At later times, it continues to decay, as the kinetic energy flux required to maintain the expansion of the tamper and internal absorber exceeds the absorbed ion-energy flux. This maximum pressure also represents the limiting shock pressure that can be induced in the payload. To increase this pressure, we need to increase the ion-beam power as suggested by Eq. (15) [increasing m_P will increase t_0 and decreasing $x_P(0)$ will reduce α].

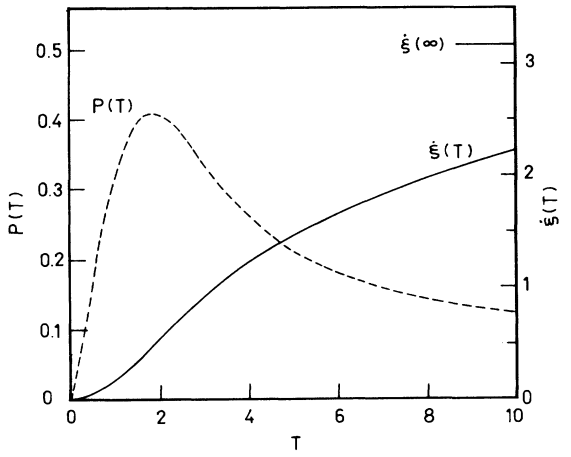

FIG. 3. Dimensionless pressure $P(T)$ and dimensionless velocity $\dot{\xi}(T)$.

Obviously, the time of peak pressure also represents the time of maximum acceleration of the payload. However, if the ion-beam power is maintained, the payload velocity will continue to increase as the payload is propelled by the expanding internal absorber. This is the regime of flyer acceleration whereby the impact momentum $\rho_P v_P^2$ of the payload can be increased by increasing the deposition of ion energy in the tamper and internal absorber. The solution of $\dot{\xi}(T)$ given in Fig. 3 corresponds to an ion-beam duration of $10t_0$. Also indicated in the figure is the asymptotic value $\dot{\xi}(\infty)$. The phenomenon of impact is well known. For an impact (flyer) velocity of v_0, the pressure of the shock induced in both the flyer and the impacted sample is given by[28]

$$P_{\rm im}=\frac{\rho_0 v_0^2}{1-(\rho_0/\rho_1)}\left[1+\left[\frac{\rho_0[1+(\rho_0'/\rho_1')]}{\rho_0'[1-(\rho_0/\rho_1)]}\right]^{1/2}\right]^{-2}\ , \tag{16}$$

where ρ_0 and ρ_0' are, respectively, the densities of the unshocked flyer and sample, and ρ_1 and ρ_1' correspond to that of the flyer and sample at pressure $p_{\rm im}$. The solution of this equation can be found when the Hugoniot equations[29] for the flyer and sample materials are known.

To elucidate on the design of flyer targets for light-ion beams, we considered the specific example of generating ultrahigh pressures in an impacted gold sample using a 3-MeV proton beam. Five different target configurations have been examined. The parameters listed in Table I

TABLE I. Targets for ultrahigh-pressure generation in gold.

Target	Tamper (μm)	Internal absorber (μm)	Payload (μm)	t_0 (ns)
A	Au 31.1	Au 31.1	Au 8.2	1.74
B	Au 21	CH_2 19	Au 5.5	1.90
C	Al 44.4	CH_2 40.3	Au 2.5	2.11
D	Al 44.4	CH_2 40.3	Al 17.5	2.11
E	Al 44.4	CH_2 40.3	Cu 5.3	2.11

($A-E$) represent the optimal design in each case. The resulting impact pressures in gold are presented in Fig. 4. Here, we have arbitrarily taken impact to occur when the payload has been propelled over a distance of 500 μm. This distance is much less than the typical diameter of ion beams on target (e.g., ~ 3 mm for the case in Ref. 11) so that the one-dimensional model is justified. For optimal use of the ion-beam energy, the calculations also assumed that the pulse duration t_B of the ion beam is equal to $t_{\rm im}$, the time required to propel the payload over 500 μm. That is, all the beam energy will be deposited in the target when the payload impacts on the sample. For the five targets considered, $t_{\rm im} \simeq 10 t_0$. Accordingly, $t_B \simeq 20$ ns for $W_0 = 10^{11}$ W/cm^2 and $t_B \simeq 4$ ns for $W_0 = 10^{13}$ W/cm^2 [as indicated by Eq. (10), t_0 and hence t_B scale as $W_0^{1/3}$]. As a base reference, the calculation was first performed for a uniform target (target A). Interestingly, even for an ion-beam flux of 10^{11} W/cm^2, which has been demonstrated in existing machines,[11] a shock pressure of ~ 5 Mbars can be achieved in the impacted sample. There are three possibilities to increase this pressure: (i) increase the hydrodynamic efficiency η_H of the target, (ii) increase the impact momentum of the payload, and (iii) use the shock reflection via impedance mismatch.[12]

The hydrodynamic efficiency can be readily increased using an external tamper[14,17] (Fig. 1). For target B, with a gold tamper and a CH_2 internal absorber, $\eta_H = 0.23$ (as compared with an hydrodynamic efficiency of 0.17 for the uniform target) leading to an almost twofold improvement in the impact pressure.

For a given η_H (or payload kinetic energy), the impact momentum of the payload can be increased by reducing m_P. However, m_P cannot be changed arbitrarily without affecting η_H. To maintain a reasonable η_H, the total mass of the target has to be reduced while reducing m_P. This can be achieved using a lighter tamper (target C), which yielded an η_H of 0.18 only but a nearly threefold increase in the impact pressure over the uniform target case.

To examine the use of shock reflection as a means of enhancing the impact pressure, we first considered aluminum as the payload or flyer material, while keeping the same tamper and internal absorber at target C, that is, keeping the same η_H and m_P. The mismatch in shock impedance between aluminum and gold caused a strong shock reflection at the impact interface. Unfortunately, the much lower density of the payload led to a decrease in its impact momentum which more than offset the gain derived from impedance mismatch (target D in Fig. 4). One might try to reduce the loss in impact momentum using a payload of intermediate densities such as copper (target E in Table I). However, the resulting impact pressure remained below that which could be obtained using target C (Fig. 4).

Thus, the optimal target to be used as an ion-beam-driven flyer would incorporate an external tamper to improve hydrodynamic efficiency, and a high-density but low-mass payload to increase impact momentum. This is basically the configuration used in target C. For this particular example, one may try to further reduce the payload mass at the expense of decreasing the hydrodynamic efficiency (due to the low-density tamper required). This may allow one to reach the ultimate impact pressure. However, the mass and therefore the thickness of the payload also govern the duration for shock loading in the impacted sample. On impact, the reflected shock will propagate backwards through the payload. When it reaches the lower-density internal absorber, a rarefaction wave is launched at the payload-absorber interface, which then propagates into the payload and the impacted sample, leading to shock attenuation.[28] For the sample to be free from such an attenuation effect, the shock loading duration can be estimated as the round-trip acoustic transit time in the payload. In practical applications, one might trade off pressure for shock-loading duration (see, for example, targets A, B, and C in Table I).

As noted earlier, our calculation assumed that impact occurred when the payload was moved a distance of 500 μm. It is also clear that at later times, the payload velocity continues to increase towards its asymptotic value $v_P(\infty)$ (Fig. 5) as the absorber continues to expand. One

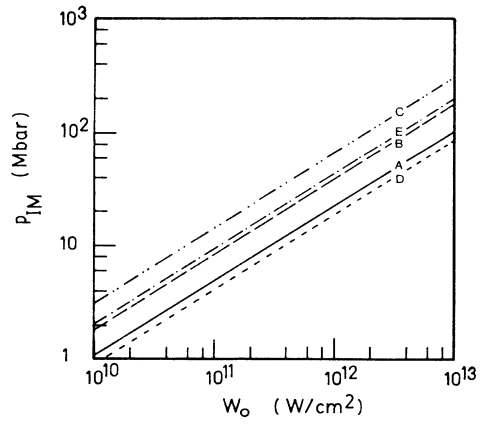

FIG. 4. Impact pressure in gold as a function of ion-beam power density.

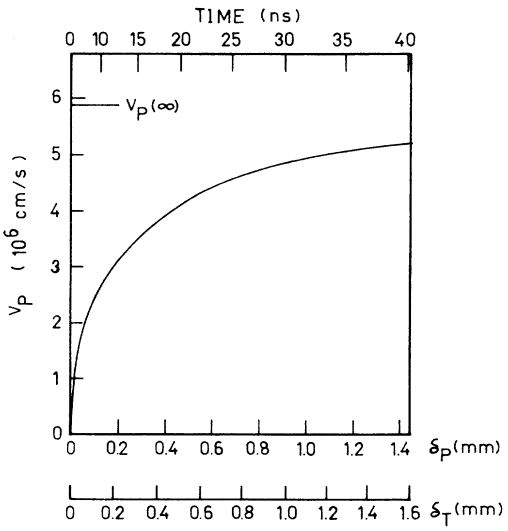

FIG. 5. V_P, as a function of time, δ_P and δ_T, for target C, and an ion-beam density of 10^{11} W/cm^2.

might therefore achieve even higher impact pressure by allowing a longer duration of payload acceleration. However, an increase in this duration implies a corresponding increase in the distance over which the payload is accelerated. If this distance becomes too large, two-dimensional effects will dominate and a one-dimensional analysis is no longer valid. For the particular example of target C, the dependence of the payload velocity v_P on the excursion distance δ_P of the accelerated payload is presented in Fig. 5. To justify the use of a one-dimensional model, one needs to examine also the distance δ_T over which the front surface of the external tamper has moved during the time of acceleration of the payload. This has been calculated for the case of target C and the results are included in Fig. 5. In experiments, δ_T should also be limited to less than the diameter of the ion beam on target to ensure a planar expansion of the tamper.

In experimental applications, the stability of the accelerating payload has to be considered as well. The acceleration of a planar foil by ion beams as described by the present model does not take into account the increase in payload mass due to shortening of the ion range[30,31] and the ablation driven by thermal radiation.[32–35] These two processes compensate each other and can be neglected in the description of the payload motion.[14,22,31] However, the ablation process must be considered in the analysis of Rayleigh-Taylor instability.[31,35]

For an ablating plasma, the Rayleigh-Taylor growth rate γ was found to be[35]

$$\gamma = 0.9\sqrt{kg} - 3kV_a \ , \tag{17}$$

where k is the perturbation wave number, g is the acceleration, and V_a is the ablation velocity. The maximum growth rate occurs when $k = 2.25\times10^{-2} g/V_a^2$ and it is

$$\gamma_{\max} = 0.068 g/V_a \ . \tag{18}$$

To estimate V, the results from free-flow ablation[32,35] is used:

$$V_a(\text{cm/s}) = 5.5\times10^4[I_R^{1/6}(\text{W/cm}^2)] \times[\tau_p^{1/12}(\text{ns})]Z^{1/12}[(1+Z)/A]^{11/24} \ , \tag{19}$$

where Z and A are the ionization state and atomic mass number of the plasma, τ_p is the pulse duration, and $I_R = \sigma T_R^4$ ($\sigma = 5.67\times10^{-5}$ erg/cm^2 s K^4 and T_R is the radiation temperature of the internal absorber) is the thermal radiation flux. For the targets considered here, $T_R \geq 4$ eV and $\tau_p = 20$ ns. Thus $V_a \geq 6\times10^5$ cm/s. It should be noted that this velocity estimate may be pessimistic since the ion-beam-driven foil acceleration scheme described here involves tamped-flow ablation, which is expected to yield a more efficient ablation process than free-flow ablation.

The acceleration of the payload is given by $g = dv_P/dt = p_P/m_P$ [Eq. (13)]. For $p_P = 1$ Mbar and $m_P \geq 5$ mg, $g \leq 2\times10^{14}$ cm/s. Accordingly, from Eq. (18), $\gamma_{\max} < 2.2\times10^7$ s^{-1} and the shortest e-folding time $\tau_{RT} = \gamma_{\max}^{-1} > 44$ ns, which exceeds the pulse duration of 20 ns. Therefore the ablation driven by thermal radiation will be an efficient stabilization mechanism for Rayleigh-Taylor instability.

On the other hand, the ablation pressure is[32]

$$P_a(\text{Mbar}) = 9.5\times10^{-11}[I_R^{5/6}(\text{W/cm}^2)] \times\tau_p^{-1/12}Z^{-1/12}[A/(1+Z)]^{11/24} \ . \tag{20}$$

For similar parameters, $P_a = 55$ kbars, which is much smaller than p_P. Thus, the ablation effect on the payload motions is indeed negligible.

One other factor that can affect the performance of the proposed ion-beam accelerated-flyer scheme is the lateral spatial nonuniformity of the focused ion beam. Such beam nonuniformities will give rise to spatially nonuniform acceleration of the flyer. Lacking detailed information on the uniformity of actual ion beams and a two-dimensional model, proper analysis of the problem and the uniformity requirements could not be made. On the other hand, it is expected that sufficient radiation smoothing may occur in the absorber to maintain uniformity in the beam-target interaction.[11]

To further illustrate the utility of ion-beam-driven flyer for ultrahigh-pressure generation, we have extended our calculation to include sample materials of various densities. For comparison purposes, we adopted the optimal flyer-impact scheme corresponding to the case of target C, namely, a symmetric impact with 44.4 μm aluminum as the tamper and 40.3 μm CH_2 as the internal absorber. We again considered a 20-ns pulse of 3-MeV proton beam with power density of 10^{11} W/cm^2. The payload thicknesses in each case are (i) Be, 33.7 μm; (ii) Ti, 10.4 μm; (iii) Cr, 6.6 μm; (iv) Cu, 5.3 μm; and (v) Ta, 2.8 μm. Since the configuration of the tamper and internal absorber and the mass of the payload are the same as in target C, the dependence of the velocity of the accelerated payload on time, δ_P and δ_T, will be identical to that presented in Fig. 5. On the other hand, the impact momentum will depend on the payload density. Figure 6 shows the pressures achieved in the different samples. We have also taken impact to occur when the payload

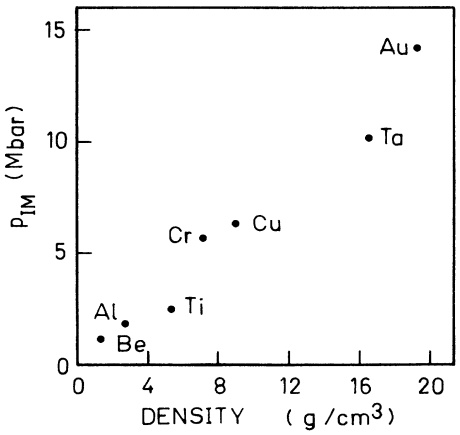

FIG. 6. Impact pressure as a function of sample material density for an ion-beam power density of 10^{11} W/cm^2.

has been accelerated over a distance of 500 μm but after the end of the ion-beam pulse. As is well known in impact phenomena, the impact pressure increases with the density of the impacted sample.

In conclusion, through a simple analytical model, we have examined and demonstrated the feasibility of ultrahigh-pressure generation using light-ion beams for flyer acceleration and impact. With proper target designs, pressures in excess of 5 Mbars can be produced in materials with densities greater than ~ 7 g/cm^3, even at a power density of 10^{11} W/cm^2, which is attainable with existing machines, and even when the acceleration of the flyer (payload) is restricted to a distance of 500 μm. This, coupled with the mm-size diameter of the ion beam on target, and the lack of a high-temperature plasma corona, renders light-ion beams potentially one of the most important tools for laboratory high-pressure research.

This work is supported by the Natural Sciences and Engineering Research Council of Canada. A.R.P. received financial support from the University of Buenos Aires, Argentina.

---

*Present address: Consejo Nacional de Investigaciones y Técnicas, Argentina.

[1]A. Jayaraman, Rev. Mod. Phys. **55**, 65 (1983).
[2]L. V. Al'tshuler, Usp. Fiz. Nauk. **85**, 197 (1965) [Sov. Phys.—Usp. **8**, 52 (1965)].
[3]A. C. Mitchell and W. J. Nellis, J. Appl. Phys. **52**, 3363 (1981).
[4]C. E. Ragan III, Phys. Rev. A **29**, 1391 (1984).
[5]L. Veeser and J. Solem, Phys. Rev. Lett. **40**, 1391 (1978).
[6]R. J. Trainor, J. W. Shaner, J. M. Auerbach, and N. C. Holmes, Phys. Rev. Lett. **42**, 1154 (1979).
[7]R. J. Trainor, N. C. Holmes, R. A. Anderson, E. M. Campbell, W. C. Mead, R. J. Olness, R. E. Turner, and F. Ze, Appl. Phys. Lett. **43**, 542 (1983).
[8]F. Cottet, J. P. Romain, R. Fabbro, and B. Faral, Phys. Rev. Lett. **52**, 1884 (1984).
[9]R. E. Kidder, *Physics of High Density,* edited by P. Caldirola and H. Knoepfel (Academic, New York, 1971), p. 306.
[10]D. L. Hanson and M. K. Matzen, *Shock Waves in Condensed Matter,* edited by S. C. Schmidt and N. C. Holmes (Elsevier Science, New York, 1988), p. 777.
[11]K. Imasaki, S. Miyamoto, N. Yugami, T. Akiba, S. Sawada, K. Emura, Y. Mizuguchi, K. Shimoura, K. Nishihara, T. Ozaki, S. Nakai, and C. Yamanaka, Laser Particle Beams **5**, 609 (1987).
[12]W. J. Nellis, *High Pressure Measurement Techniques,* edited by G. N. Peggs (Applied Science, New York, 1983), Chap. 2.
[13]A. R. Piriz, Phys. Fluids **31**, 658 (1988).
[14]N. Metzler and J. Meyer-Ter-Vehn, Laser Particle Beams **2**, 27 (1984).
[15]N. A. Tahir and K. A. Long, Z. Phys. A **325**, 99 (1986).
[16]G. Velarde, J. M. Aragones, J. A. Gago, L. Games, M. C. Gonzales, J. J. Honrubia, J. L. Hortal, J. Martinez-Val, E. Miguez, J. L. Ocaña, R. Otero, J. M. Perlado, J. M. Santolaya, J. F. Serrano, and P. M. Velarde, Laser Particle Beams **4**, 349 (1986).
[17]C. R. Devore, J. H. Gardner, J. P. Boris, and D. Mosher, Laser Particle Beams **2**, 227 (1984).
[18]K. A. Long, and N. A. Tahir, Phys. Fluids **29**, 275 (1986); **29**, 4204 (1986).
[19]A. V. Farnsworth, M. M. Widner, M. J. Clauser, P. J. Daniel, and K. E. Lonngren, Phys. Fluids **22**, 859 (1979).
[20]P. C. Thompson, P. D. Roberts, N. J. Freeman, and P. T. G. Fynn, J. Phys. D **14**, 1215 (1981).
[21]R. G. Evans, Laser Particle Beams **1**, 231 (1983).
[22]N. A. Tahir, and K. A. Long, Nucl. Fusion **23**, 887 (1983).
[23]L. C. Northcliffe and R. F. Schilling, Nucl. Data Tables A **7**, 233 (1970).
[24]F. Hubert, A. Fleury, R. Bimbot, and D. Gardes, Suppl. Ann. Phys. (Paris) **5**, 1 (1980).
[25]J. F. Ziegler, *Handbook of Stopping Cross-Section for Energetic Ions in All Elements* (Pergamon, New York, 1980), Vol. 5.
[26]U. Littamark and J. F. Ziegler, *Handbook of Range Distributions for Energetic Ions in All Elements* (Pergamon, New York, 1980), Vol. 6.
[27]Sandia National Laboratories 1980 Particle Beam Fusion Facility Report No. SAND80-0006 (unpublished).
[28]J. W. Gehring, Jr., *High Velocity Impact Phenomena,* edited by R. Kinslow (Academic, New York, 1970), Chap. IV.
[29]R. G. McQueen, S. P. March, J. W. Taylor, J. N. Fritz, and W. J. Carter, Ref. 28, Chap. VII.
[30]A. Melhorn, J. Appl. Phys. **52**, 6522 (1981).
[31]K. A. Long and N. A. Tahir, Phys. Rev. A **35**, 2631 (1981).
[32]K. Nishihara, Jpn. J. Appl. Phys. **21**, L571 (1982).
[33]K. Imasaki, S. Miyamoto, S. Higaki, T. Ozaki, S. Nakai, and C. Yamanaka, Jpn. J. Appl. Phys. **23**, L83 (1984).
[34]M. Murakami and K. Nishihara, Jpn. J. Appl. Phys. **26**, 1132 (1987).
[35]H. Takabe, K. Mima, L. Montierth, and R. L. Morse, Phys. Fluids **28**, 3676 (1985).